Available online at www.sciencedirect.com
SCIENCE DIRECT®
Comput. Methods Appl. Mech. Engrg. 195 (2006) 1885–1895
Computer methods in applied mechanics and engineering
www.elsevier.com/locate/cma

Computer modeling of cardiovascular fluid–structure interactions with the deforming-spatial-domain/stabilized space–time formulation

Ryo Torii [a,*], Marie Oshima [a], Toshio Kobayashi [b], Kiyoshi Takagi [c,1], Tayfun E. Tezduyar [d]

[a] Institute of Industrial Science, The University of Tokyo, 4-6-1 Komaba, Meguro-ku, Tokyo 153-8505, Japan
[b] Japan Automobile Research Institute, 2530 Karima, Tsukuba-shi, Ibaraki 305-0822, Japan
[c] School of Medicine, Teikyo University, 2-11-2 Kaga, Itabashi-ku, Tokyo 173-8605, Japan
[d] Mechanical Engineering, Rice University—MS 321, 6100 Main Street, Houston, TX 77005, USA

Received 12 October 2004; received in revised form 18 January 2005; accepted 26 May 2005

Tribute to Thomas J.R. Hughes on his 60th birthday

Abstract

Hemodynamic factors such as the wall shear stress are believed to affect a number of cardiovascular diseases including atherosclerosis and aneurysm. Since resolving phenomena in a living human body is currently beyond the capabilities of in vivo measurement techniques, computer modeling is expected to play an important role in gaining a better understanding of the relationship between the cardiovascular diseases and the hemodynamic factors. We have developed a computer modeling technique for cardiovascular hemodynamic simulations. With this modeling technique, patient-specific 3D geometry of an artery can be analyzed. We take into account some of the important factors in human body for the purpose of demonstrating in vivo situations in a virtual world. The interaction between the blood flow and the deformation of the arterial walls is a factor that we are specifically focusing on. For such fluid–structure interactions, we have developed a computer modeling tool based on the deforming-spatial-domain/stabilized space–time (DSD/SST) formulation. This simulation tool is applied to a patient-specific model under pulsatile blood flow conditions. The simulations show that the flow behavior with compliant arterial walls is different from what we see with rigid arterial walls. Consequently, the distribution of the wall shear stress on the compliant arterial walls is significantly different from that on the rigid arterial walls. We deduce that the compliance of the arterial walls needs to be taken into

* Corresponding author. Present address: Department of Chemical Engineering and Chemical Technology, Imperial College, London SW7 2AZ, United Kingdom. Tel.: +44 020 7589 5111.
E-mail address: r.torii@imperial.ac.uk (R. Torii).
[1] Present address: Ogura Hospital, 4-2-5 Nakamachi, Setagaya-ku, Tokyo 158-8585, Japan.

0045-7825/$ - see front matter
doi:10.1016/j.cma.2005.05.050

account in cardiovascular hemodynamic simulations, and the computer modeling tool we have developed can be effective in investigation of cardiovascular diseases.

Keywords: Cardiovascular disease; Fluid–structure interaction; DSD/SST method

1. Introduction

Over 95% of the subarachnoid hemorrhages in Japan are caused by rupture of cerebral aneurysm [1]. Fig. 1 shows an example of cerebral aneurysm. Although the rupture risk for aneurysms with diameters less than 10 mm is reported [2] to be under 0.1%, most aneurysms can be operated on if they are detected. It is also reported in [2] that the risk of postoperative sequelae is over 10%. Therefore it would be very helpful to identify the cases where the aneurysm is exposed to a high risk of rupture, and avoid unwarranted surgeries in other cases. More aneurysms are detected during physical examinations, thanks to the recent developments in medical imaging. It is reported [3] that 6% of the population in Japan have cerebral aneurysm. In earlier studies focusing on cerebral aneurysms [4], hemodynamic forces, such as the blood pressure and wall shear stress (WSS), were recognized as playing a significant role. Recently, through physiological experiments [5], it was also shown that hemodynamic factors influence other vascular diseases, such as atherosclerosis. For these reasons, we have developed a computer modeling tool to investigate the hemodynamic mechanisms involved in cardiovascular diseases. Since in vivo measurements currently cannot resolve phenomena in a living human body, computer modeling is expected to play an important role in better understanding of the relationship between the cardiovascular diseases and the hemodynamic factors.

In our computer modeling, in addition to using patient-specific arterial models [6], we take into account some of the important factors in human body to demonstrate in vivo situations in a virtual world. One of such factors that we are specifically focusing on is the interaction between the blood flow and the deformation of the arterial walls. In computer modeling of those fluid–structure interactions, we use a numerical approach based on the deforming-spatial-domain/stabilized space–time (DSD/SST) method [7–9]. Although the progress of cardiovascular diseases, such as the growth of aneurysms, is associated with both mechanical and biological factors, we focus in this paper on mechanical factors. The patient-specific model we use in this study is that of the internal carotid artery, which is one of the common aneurysmal sites. A pulsatile flow based on measured blood velocity profile is used as inflow boundary condition in the com-

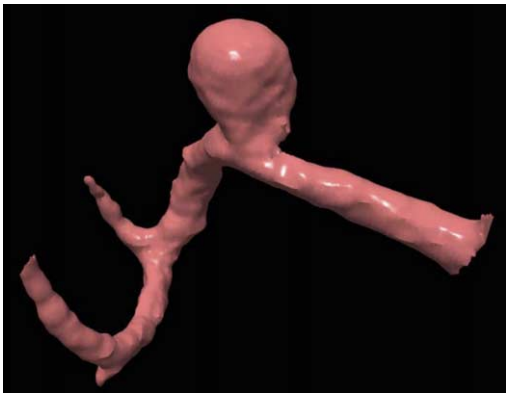

Fig. 1. A saccular aneurysm on the middle cerebral artery.

putation. We investigate the effects of elastic arterial walls on the blood flow and hemodynamic forces. To better understand the role of the interaction between the blood flow and the arterial wall motion, the results are compared with those from computations with rigid arterial walls.

2. Computational model

In this study the fluid and structural mechanics equation systems are solved with a block–iterative coupling approach. The two systems are coupled at the interface by the kinematic and dynamic conditions. The computational methods used for fluid mechanics, structural mechanics, and mesh update are described in the following subsections.

2.1. Fluid mechanics

The blood flow in cerebral arteries is assumed to be laminar [4], and it is governed by the Navier–Stokes equations of incompressible flows:

$$\rho\left(\frac{\partial \boldsymbol{u}}{\partial t}+\boldsymbol{u}\cdot\nabla\boldsymbol{u}\right)-\nabla\cdot\boldsymbol{\sigma}=0, \tag{1}$$

$$\nabla\cdot\boldsymbol{u}=0, \tag{2}$$

where ρ is the density and $\boldsymbol{u}$ is the velocity. The external forces, such as those due to gravity or human motion, are assumed to be not significant and are neglected. Although the blood is known to be non-Newtonian in general, we assume it to be Newtonian in this study. This is because we consider large arteries with radii of the order 1.0 mm, where the velocity and shear rate are high. The apparent viscosity is nearly a constant in arteries with relatively large diameters ($\sim$5 mm) [10], and therefore the non-Newtonian effects are neglected. The stress tensor is defined as

$$\boldsymbol{\sigma}(p,\boldsymbol{u})=-p\boldsymbol{I}+2\mu\varepsilon(\boldsymbol{u}), \tag{3}$$

where μ is the viscosity and $\varepsilon(\boldsymbol{u})$ is the strain-rate tensor:

$$\varepsilon(\boldsymbol{u})=\frac{1}{2}\left(\nabla\boldsymbol{u}+(\nabla\boldsymbol{u})^{\mathrm{T}}\right). \tag{4}$$

The essential and the natural boundary conditions are taken into account as

$$\boldsymbol{u}=\boldsymbol{g}\quad\text{on } \Gamma_g, \tag{5}$$

$$\boldsymbol{n}\cdot\boldsymbol{\sigma}=\boldsymbol{h}\quad\text{on } \Gamma_h, \tag{6}$$

where Γ_g and Γ_h are the complementary subset of the boundary Γ.

Eqs. (1) and (2) are discretized with the DSD/SST finite element formulation [7–9]. The DSD/SST method has been applied to a large number of problems with moving boundaries and interfaces [11,12], including fluid–structure interactions [13–15]. In the formulation, the time interval $(0,T)$ is divided into a sequence of subintervals $I_n=(t_n,t_{n+1})$. The space–time domain between Ω_n and Ω_{n+1}, which are the spatial domains at time levels t_n and t_{n+1}, is defined as the space–time slab and denoted by Q_n. The space–time boundary of Q_n is generated by the boundary Γ_t as t traverses I_n, and is denoted by P_n. The boundary P_n is decomposed into $(P_n)_g$ and $(P_n)_h$ with respect to the type of boundary conditions (essential and natural). For each space–time slab, we define the corresponding finite element trial function spaces $(\mathscr{S}^h_{\boldsymbol{u}})_n$ for velocity and $(\mathscr{S}^h_p)_n$ for pressure, and the test function spaces $(\mathscr{V}^h_{\boldsymbol{u}})_n$ and $(\mathscr{V}^h_p)_n=(\mathscr{S}^h_p)_n$. The governing equations are discretized by using four dimensional interpolation functions in the space–time domain. In this study, we use first-order polynomials in both space and time. At each time step, the finite element formulation is written over the

corresponding space–time slab. Changes in the shape of the spatial domain occupied by the fluid are represented by the shapes of the space–time slabs. No additional terms are needed for treatment of the moving boundaries. The version of the DSD/SST formulation that was introduced in [16] is written as follows: given $(\boldsymbol{u}^h)_n^-$, find $\boldsymbol{u}^h \in (\mathscr{S}_{\boldsymbol{u}}^h)_n$ and $p^h \in (\mathscr{S}_p^h)_n$ such that $\forall \boldsymbol{w}^h \in (\mathscr{V}_{\boldsymbol{u}}^h)_n$ and $\forall q^h \in (\mathscr{V}_p^h)_n$:

$$\begin{aligned}
&\int_{Q_n} \boldsymbol{w}^h \cdot \rho\left(\frac{\partial \boldsymbol{u}^h}{\partial t} + \boldsymbol{u}^h \cdot \nabla \boldsymbol{u}^h\right) \mathrm{d}Q + \int_{Q_n} \varepsilon(\boldsymbol{w}^h) : \boldsymbol{\sigma}(p^h, \boldsymbol{u}^h)\, \mathrm{d}Q - \int_{(P_n)_h} \boldsymbol{w}^h \cdot \boldsymbol{h}\, \mathrm{d}P \\
&\quad + \int_{Q_n} q^h \nabla \cdot \boldsymbol{u}^h\, \mathrm{d}Q + \int_{\Omega} (\boldsymbol{w}^h)_n^+ \cdot ((\boldsymbol{u}^h)_n^+ - (\boldsymbol{u}^h)_n^-)\, \mathrm{d}\Omega \\
&\quad + \sum_{e=1}^{(n_{el})_n} \int_{Q_n^e} \frac{1}{\rho}\left[\tau_{\mathrm{SUPG}} \rho\left(\frac{\partial \boldsymbol{w}^h}{\partial t} + \boldsymbol{u}^h \cdot \nabla \boldsymbol{w}^h\right) + \tau_{\mathrm{PSPG}} \nabla q^h\right] \\
&\quad \cdot \left[\rho\left(\frac{\partial \boldsymbol{u}^h}{\partial t} + \boldsymbol{u}^h \cdot \nabla \boldsymbol{u}^h\right) - \nabla \cdot \boldsymbol{\sigma}(p^h, \boldsymbol{u}^h)\right] \mathrm{d}Q = 0,
\end{aligned} \tag{7}$$

where the notation $(\cdot)_n^+$ and $(\cdot)_n^-$ denotes the values as t_n is approached from above and below:

$$(\phi)_n^{\pm} = \lim_{\delta \to 0} \phi|_{t=t_n \pm \delta}. \tag{8}$$

The DSD/SST formulation is applied to all space–time slabs $Q_0, Q_1, \ldots, Q_{N-1}$, starting with $(\boldsymbol{u})_0^- = \boldsymbol{u}_0$. In this formulation, the first five integrations represent the Galerkin method. The fifth term represents the approximate continuity of the velocity in time. The last term is the stabilization based on the streamline-upwind/Petrov–Galerkin (SUPG) [17,18] and pressure-stabilizing/Petrov–Galerkin (PSPG) [7,19] formulations. The stabilization parameters are denoted by τ_{SUPG} and τ_{PSPG}. There are a number of ways to define these parameters, and in this study we employ the following definitions [16]:

$$\tau_{\mathrm{SUPG}} = \left(\frac{1}{\tau_{\mathrm{SUGN12}}^2} + \frac{1}{\tau_{\mathrm{SUGN3}}^2}\right)^{-1/2}, \tag{9}$$

$$\tau_{\mathrm{SUGN12}} = \left(\sum_{a=1}^{n_{\mathrm{en}}} \left|\frac{\partial N_a}{\partial t} + \boldsymbol{u}^h \cdot \nabla N_a\right|\right)^{-1}, \quad \tau_{\mathrm{SUGN3}} = \frac{h_{\mathrm{RGN}}^2}{4\nu}, \tag{10}$$

$$h_{\mathrm{RGN}} = \left(\sum_{a=1}^{n_{\mathrm{en}}} |\boldsymbol{r} \cdot \nabla N_a|\right)^{-1}, \quad \boldsymbol{r} = \frac{\nabla \|\boldsymbol{u}\|}{\|\nabla \|\boldsymbol{u}\|\|}, \tag{11}$$

$$\tau_{\mathrm{PSPG}} = \tau_{\mathrm{SUPG}}. \tag{12}$$

Here N_a is the space–time shape function associated with the element node a, n_{en} is the number of element nodes, and ν is the kinematic viscosity. For more details on the stabilization parameters, see [16].

2.2. Structural mechanics

The governing equations for the structural mechanics are the equilibrium equations:

$$\rho^{\mathrm{s}}\left(\frac{\mathrm{d}^2 \boldsymbol{y}}{\mathrm{d}t^2} - \boldsymbol{f}^{\mathrm{s}}\right) - \nabla \cdot \boldsymbol{\sigma}^{\mathrm{s}} = 0, \tag{13}$$

where the superscript s denotes the structure, $\boldsymbol{y}$ is the displacement vector, ρ^{s} is the density of the material, $\boldsymbol{f}^{\mathrm{s}}$ represents the external body forces acting on the structure, and $\boldsymbol{\sigma}^{\mathrm{s}}$ is the Cauchy stress tensor. Although

the arterial wall is known to be made of elastic material that is nonlinear, we assume it to be linear in this study. We use Galerkin finite element formulation based on the following principle of virtual work:

$$\int_{\Omega_0^s} \boldsymbol{w} \cdot \rho^s \frac{\mathrm{d}^2 \boldsymbol{y}}{\mathrm{d}t^2}\,\mathrm{d}\Omega + \int_{\Omega_0^s} \delta \boldsymbol{E} : \boldsymbol{S}\,\mathrm{d}\Omega = \int_{\Gamma_t^s} \boldsymbol{w} \cdot \boldsymbol{t}\,\mathrm{d}\Gamma + \int_{\Omega_t^s} \boldsymbol{w} \cdot \rho^s \boldsymbol{f}^s\,\mathrm{d}\Omega. \tag{14}$$

Here $\boldsymbol{S}$ is the 2nd Piola–Kirchoff stress tensor, $\boldsymbol{E}$ is the Cauchy–Green strain tensor, and the test function $\boldsymbol{w}$ is also the virtual displacement. The fluid dynamics forces are included in the traction vector $\boldsymbol{t}$. Using the Newmark-β method [20] for time-integration, a nonlinear system of equations is obtained at each time step and can be written in the incremental form as

$$\left(\frac{1}{\beta \Delta t^2}\boldsymbol{M} + \boldsymbol{K}\right)\Delta \boldsymbol{Y}^{\,i} = \boldsymbol{R}^i. \tag{15}$$

Here $\boldsymbol{Y}$ is the vector of nodal values of $\boldsymbol{y}$, $\boldsymbol{M}$ is the global mass matrix, $\boldsymbol{K}$ is the tangent stiffness matrix, $\boldsymbol{R}^i$ is the residual vector at the ith iteration, $\Delta \boldsymbol{Y}^i$ is the ith increment in the vector $\boldsymbol{Y}$, and Δt is the time step size. The parameters β and γ control the stability and accuracy of the method. We use $\beta = 0.3225$ and $\gamma = 0.6$ in our study.

2.3. Mesh update

The fluid mesh is updated by using an automatic mesh moving method [21]. In this method the motion of the nodes is governed by the equations of elasticity. The boundary conditions come from the motion of the interface between the fluid and structure.

2.4. Fluid–structure coupling

The fluid and structural mechanics equations are coupled by a block–iterative coupling method. We define the fluid and structural nodes at the interface to be the same. Thus the data for each nodal point at the interface can be exchanged directly between the fluid and structure. The fluid forces at the interface are treated as external forces for the structure. In return, structural displacements at the interface are treated as essential boundary conditions for the fluid dynamics in the DSD/SST formulation. In block–iterative coupling of the fluid and structural mechanics equations, the structural response becomes very sensitive to small changes in the fluid dynamics forces. We perform several iterations within each time step to avoid potential convergence problems, which were pointed out in [22].

3. Numerical example

3.1. Patient-specific model of the intracranial arteries

A computer simulation procedure based on medical imaging data was developed in [6] for arterial blood flow. In this procedure, 3D geometries of arteries are extracted from computed tomography (CT) with the commercial software ALATOVIEW. The patient-specific model we use as numerical example is that of the internal carotid artery. This artery is one of the common sites of cerebral aneurysm. The diameter of the artery is approximately 4.0 mm. The patient is a male in his 70s. We investigate the interaction between the blood flow and the arterial-wall deformation in a sharply curved artery. The model geometry and the mesh are shown in Fig. 2. The number of fluid and structural nodes are 29,643 and 11,808, respectively. The number of fluid and structural elements are 23,708 and 7808, respectively. The mesh was generated with the commercial software ICEM CFD.

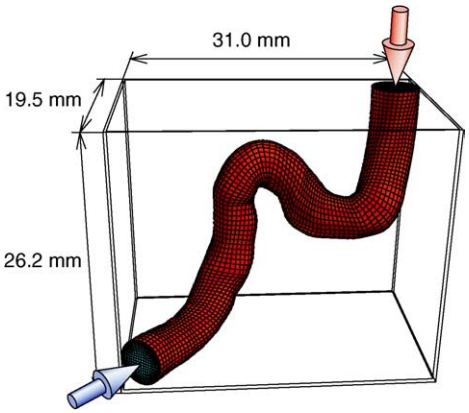

Fig. 2. Geometry of the computational model (blue arrow: inflow, red arrow: pressure resistance of the downstream arterial network).

3.2. Boundary conditions and initial condition

The inflow boundary condition is a pulsatile velocity profile described with the following Womersley solution of pulsatile flow [23]:

$$w(r,t) = \frac{2B_0}{\pi R^2}\left[1-\left(\frac{r}{R}\right)^2\right] + \sum_{n=1}^{N}\frac{B_n}{\pi R^2}\left[\frac{1-\dfrac{J_0(\alpha_n \frac{r}{R} \mathrm{i}^{3/2})}{J_0(\alpha_n \mathrm{i}^{3/2})}}{1-\dfrac{2J_1(\alpha_n \mathrm{i}^{3/2})}{\alpha_n \mathrm{i}^{3/2} J_0(\alpha_n \mathrm{i}^{3/2})}}\right] \mathrm{e}^{\mathrm{i}n\omega t}, \tag{16}$$

$$Q(t) = \sum_{n=0}^{N} B_n \mathrm{e}^{\mathrm{i}\omega t}. \tag{17}$$

Here r is the cylindrical coordinate, R denotes the radius of the inlet cross-section, and J_0 and J_1 are the Bessel functions of the first kind of order 0 and 1. The non-dimensional parameter $\alpha = R\sqrt{\omega/\nu}$ is known as the Womersley number, and $\alpha_n = R\sqrt{n\omega/\nu}$, where ω is the frequency based on one cardiac cycle (=1.0 s). The Fourier coefficients B_n are determined from the velocity profile measured by ultrasound Doppler velocimetry at the carotid artery of a male in his 20s. The order of the series is 20. The pressure resistance due to the downstream arterial network is modeled by the Windkessel model [24] as a traction boundary condition for the fluid equations. In the Windkessel model of the arterial network, the pressure, flow rate and flow resistance are seen as the voltage, current and resistance in an electric circuit. The pressure is determined by integrating the following equation:

$$Q = C\frac{\mathrm{d}p}{\mathrm{d}t} + \frac{p}{D}, \tag{18}$$

where Q is the flow rate in the artery, C is the compliance of the artery, and D is the resistance of the distal arterial network. The parameters C and D are determined in an ad hoc fashion for the pressure to range from 80 mm Hg to 120 mm Hg, which is the standard range of blood pressure for a healthy human. The transient behavior of the inflow boundary condition and the downstream pressure are shown in Fig. 3. It can be observed that the Womersley solution for the flow rate represents the measured value well. The initial condition is the fully developed flow field, computed with rigid arterial walls and by specifying an inflow condition corresponding to the beginning of the pulsatile boundary condition cycle.

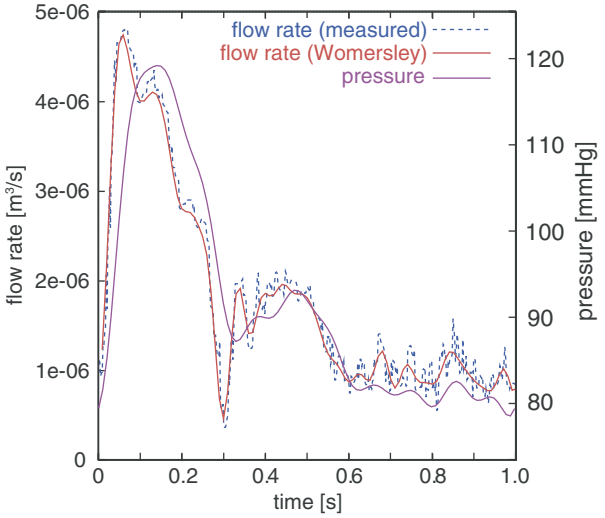

Fig. 3. Transient behavior of the boundary conditions.

In the structural calculations, both the upstream and downstream ends of the artery are fixed by means of zero-displacement boundary condition. The initial displacements and stresses are set to zero.

3.3. Determination of mechanical properties

The density and kinematic viscosity are specified as $1000\,\mathrm{kg/m^3}$ and $4.0\times10^{-6}\,\mathrm{m^2/s}$. To specify the apparent elastic modulus, we carried out a simple numerical test. We investigated the relationship between the radius and inner pressure of a straight pipe, which is assumed to be the straight portion of an artery. By comparing this to experimental data [25], we set the elastic modulus $E = 1.0$ MPa. The Poisson's ratio is set to 0.49.

3.4. Results

Fig. 4 shows the deformation of the artery. The transparent geometry shows the initial configuration at the beginning of the systole, and the geometry with the color contours show the configuration at the peak systole. The color contours depict the magnitude of the displacement. The blood flows from left to right in the figure. Since the artery is fixed at both the downstream and upstream ends of the computational domain, it is reasonable that the maximum displacement is observed in the area between the two ends. The magnitude of the maximum displacement is 0.815 mm, which is about 1/5 of the diameter. It is also observed that the displacement of the centerline is larger than the change in the arterial radius. This means that the pulsatile flow does not contribute to the expansion of the artery as much as it contributes to the deformation of the arterial axis.

Figs. 5 and 6 show the WSS distributions for the elastic and rigid wall models at the peak systole. The maximum magnitude of the WSS is 139 dyn/cm^2 for the elastic wall model and 186 dyn/cm^2 for the rigid wall model. In addition to a quantitative difference between the WSS for the two models there is a general difference in the WSS distributions. The differences in the location of the concentrated WSS are particularly remarkable because high values of the WSS are believed to affect cardiovascular diseases [5], including cerebral aneurysm. The differences in the overall WSS distributions come from the interaction between the motion of the arterial wall and the blood flow.

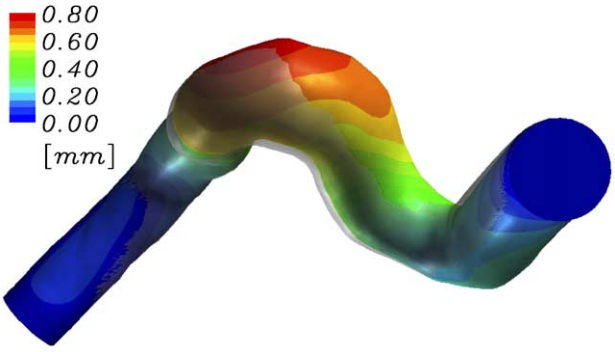

Fig. 4. Deformation of the artery at the peak systole (color contours describe the magnitude of the displacement, with the transparent geometry showing the configuration at the beginning of the systole).

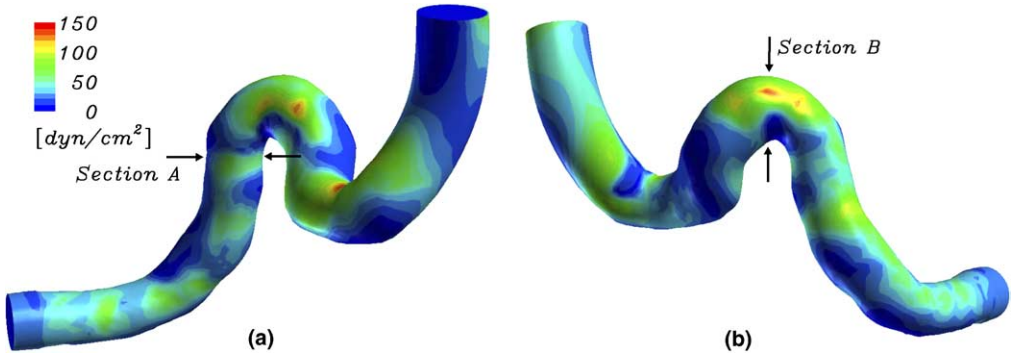

Fig. 5. WSS distribution for the elastic wall model at the peak systole. (a) Medial view, (b) lateral view.

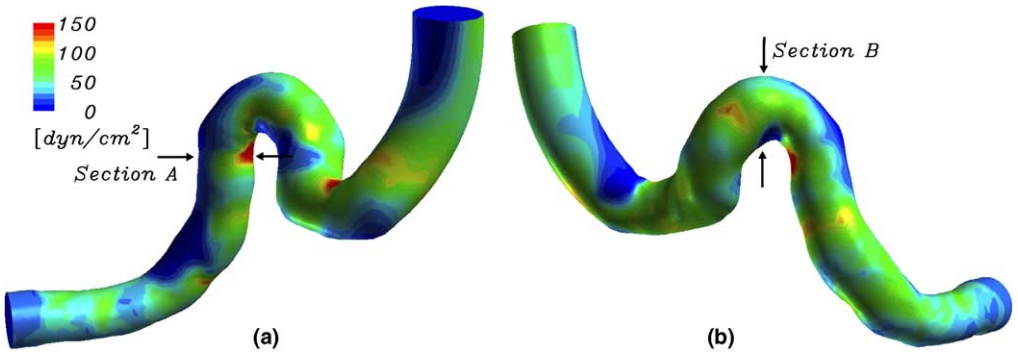

Fig. 6. WSS distribution for the rigid wall model at the peak systole. (a) Medial view, (b) lateral view.

To better understand the reasons behind the differences in the WSS distributions, we focus on the flow velocity distributions. Figs. 7–10 show the transient behavior of the velocity distributions for the elastic and rigid wall models. Sections A and B are located where we have concentrated WSS (see Figs. 5 and 6 for those locations). The systolic cycle begins at $t = 0.0$ s and ends at around $t = 0.8$ s. Because the Womersley velocity profile at the inlet section is nearly a parabolic one, a fairly parabolic profile can be seen also in

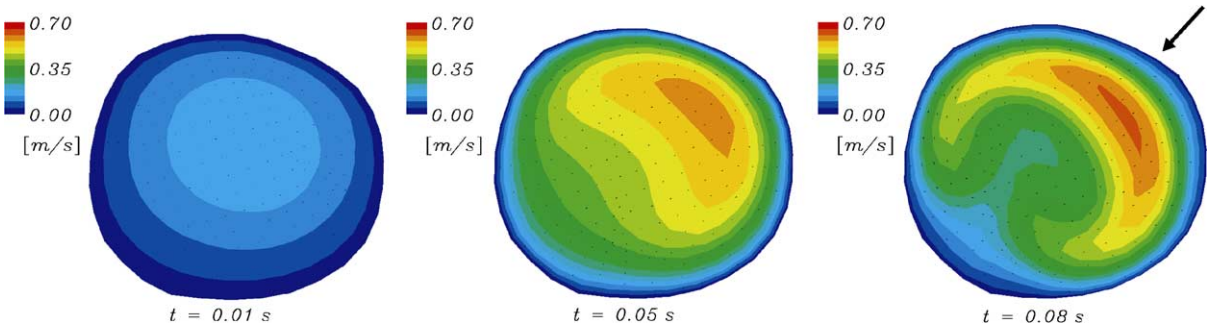

Fig. 7. Transient behavior of the velocity distribution in Section A for the elastic wall model.

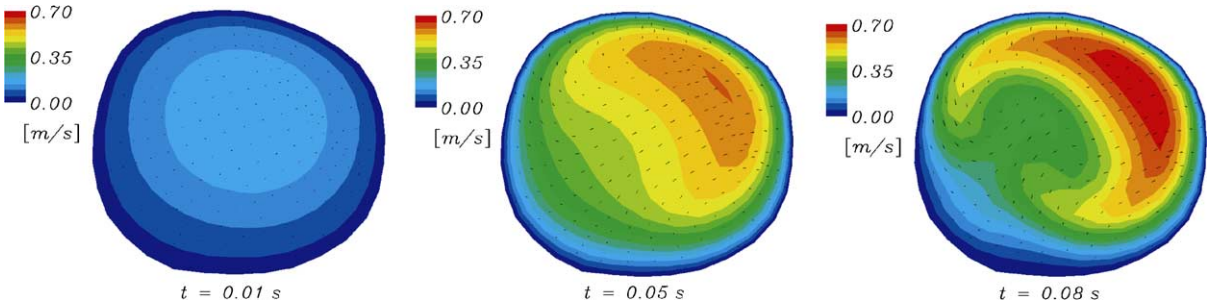

Fig. 8. Transient behavior of the velocity distribution in Section A for the rigid wall model.

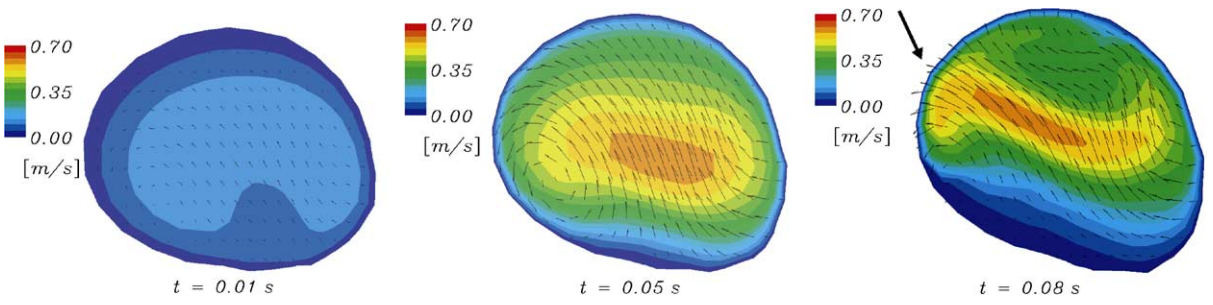

Fig. 9. Transient behavior of the velocity distribution in Section B for the elastic wall model.

Section A at $t = 0.01$ s. As time progresses, the area of high velocity magnitude takes a crescent-like shape and approaches the arterial wall. This yields high velocity magnitude near the wall, resulting in high WSS there. By comparing Figs. 7 and 8, it can be seen that the magnitude and gradient of the velocity near the wall, especially around the area indicated by an arrow in Fig. 7, are significantly smaller for the elastic wall model. When the deformation of the arterial wall is taken into account, the cross-sectional area is enlarged by the systolic increase of the pressure, and the mean velocity magnitude, therefore, decreases. In this particular case, the area at Section A for the elastic wall model is 6% larger than it is for the rigid wall model. In addition to the expansion of the cross-sectional area, the motion of the entire Section A towards the top of the figure moves the arterial wall away from the area of high velocity magnitude. This is the reason why the magnitude of the WSS around Section A in the elastic wall model is smaller than it is in the rigid wall

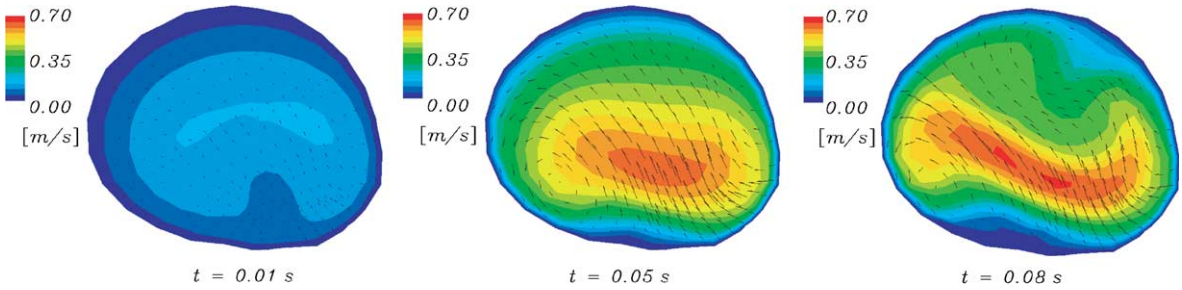

Fig. 10. Transient behavior of the velocity distribution in Section B for the rigid wall model.

model. On the other hand, around Section B the magnitude of the WSS in the elastic wall model is larger than it is in the rigid wall model. Although the velocity distributions are similar in both models at the beginning of the systolic period, the locations of the areas with high velocity magnitude are different at the peak systole. The magnitude of the velocity gradient is larger in the elastic wall model around the area indicated by an arrow in Fig. 9. The magnitude of the WSS around this area in the elastic wall model is consequently larger than it is in the rigid wall model.

4. Conclusions

We have developed a computer simulation tool based on the DSD/SST method to investigate the fluid–structure interactions between the blood flow and the arterial-wall deformation. This simulation tool has been applied to a patient patient-specific model of the cerebral artery. The results show that the WSS distributions are affected by the arterial-wall deformations. Since the WSS distribution is key to investigation of cardiovascular diseases, these results show that the computer model developed in this paper can be an effective tool in conducting hemodynamic studies of cardiovascular diseases. In the present study the arterial wall is assumed to be made of linearly elastic material. The influence of the nonlinear elastic behavior of the arterial wall on the WSS distribution remains to be investigated. As part of our future work, we will take those nonlinear effects into account by using a hyper-elastic model for the arterial wall.

Acknowledgments

Part of this research was carried out within the framework of the project "Frontier Simulation Software for Industrial Science (FSIS)", supported by the IT program of the Ministry of Education, Culture, Sports, Science and Technology (MEXT). The authors are grateful to Dr. Motoharu Hayakawa, Fujita Health University, for providing the CT data, and to Toshiba Medical, Inc. for providing the software "ALATOVIEW".

References

[1] Y. Komatsu, S. Yasuda, T. Shibata, Y. Ono, A. Hyodo, T. Nose, Management for subarachnoid hemorrhage with negative initial angiography, Neurolog. Surg. 22 (1994) 43–49 (in Japanese).
[2] The International Study of Unruptured Intracranial Aneurysms Investigators. Unruptured intracranial aneurysms—risk of rupture and risks of surgical intervention, New Engl J Med 339 (24) (1998) 1725–1733.

[3] T. Nakagawa, K. Hayashi, The incidence and treatment of asymptomatic, unruptured cerebral aneurysms, J. Neurosurg. 80 (1994) 217–223.
[4] T. Karino, S. Takeuchi, N. Kobayashi, M. Motomiya, S. Mabuchi, Fluid dynamics of cerebrovascular disease, Neurosurgeons 12 (1993) 15–24 (in Japanese).
[5] A.M. Malek, S.L. Alper, S. Izumo, Hemodynamic shear stress and its role in atherosclerosis, J. Amer. Med. Assoc. 282 (1999) 2035–2042.
[6] R. Torii, M. Oshima, T. Kobayashi, K. Takagi, The hemodynamic study of the cerebral artery using numerical simulations based on medical imaging data, J. Visual. 4 (3) (2001) 277–284.
[7] T.E. Tezduyar, Stabilized finite element formulations for incompressible flow computations, Adv. Appl. Mech. 28 (1992) 1–44.
[8] T.E. Tezduyar, M. Behr, J. Liou, A new strategy for finite element computations involving moving boundaries and interfaces—the deforming-spatial-domain/space–time procedure: I. The concept and the preliminary numerical tests, Comput. Methods Appl. Mech. Engrg. 94 (3) (1992) 339–351.
[9] T.E. Tezduyar, M. Behr, S. Mittal, J. Liou, A new strategy for finite element computations involving moving boundaries and interfaces—the deforming-spatial-domain/space–time procedure: II. Computation of free-surface flows, two-liquid flows, and flows with drifting cylinders, Comput. Methods Appl. Mech. Engrg. 94 (3) (1992) 353–371.
[10] D.A. McDonald, Blood Flow in Arteries, second ed., Edward Arnold, 1974.
[11] T.E. Tezduyar, Finite element methods for flow problems with moving boundaries and interfaces, Arch. Comput. Methods Engrg. 8 (2001) 83–130.
[12] T.E. Tezduyar, Finite element methods for fluid dynamics with moving boundaries and interfaces, in: E. Stein, R. De Borst, T.J.R. Hughes (Eds.), Encyclopedia of Computational Mechanics, Fluids, vol. 3, John Wiley & Sons, 2004 (Chapter 17).
[13] K. Stein, R. Benney, V. Kalro, T.E. Tezduyar, J. Leonard, M. Accorsi, Parachute fluid–structure interactions: 3-D computation, Comput. Methods Appl. Mech. Engrg. 190 (2000) 373–386.
[14] K. Stein, R. Benney, T. Tezduyar, J. Potvin, Fluid–structure interactions of a cross parachute: numerical simulation, Comput. Methods Appl. Mech. Engrg. 191 (2001) 673–687.
[15] K.R. Stein, R.J. Benney, T.E. Tezduyar, J.W. Leonard, M.L. Accorsi, Fluid–structure interactions of a round parachute: Modeling and simulation techniques, J. Aircraft 38 (2001) 800–808.
[16] T.E. Tezduyar, Computation of moving boundaries and interfaces and stabilization parameters, Int. J. Numer. Methods Fluids 43 (2003) 555–575.
[17] T.J.R. Hughes, A.N. Brooks, A multi-dimensional upwind scheme with no crosswind diffusion, in: T.J.R. Hughes (Ed.), Finite Element Methods for Convection Dominated Flows, AMD-vol. 34, ASME, New York, 1979, pp. 19–35.
[18] A.N. Brooks, T.J.R. Hughes, Streamline upwind/Petrov–Galerkin formulations for convection dominated flows with particular emphasis on the incompressible Navier–Stokes equations, Comput. Methods Appl. Mech. Engrg. 32 (1982) 199–259.
[19] T.E. Tezduyar, S. Mittal, S.E. Ray, R. Shih, Incompressible flow computations with stabilized bilinear and linear equal-order-interpolation velocity–pressure elements, Comput. Methods Appl. Mech. Engrg. 95 (1992) 221–242.
[20] N.M. Newmark, A method of computation for structural dynamics, ASCE J. Engrg. Mech. 85 (1959) 67–94.
[21] T.E. Tezduyar, M. Behr, S. Mittal, A.A. Johnson, Computation of unsteady incompressible flows with the finite element methods—space–time formulations, iterative strategies and massively parallel implementationsNew Methods in Transient Analysis, PVP-vol. 246/AMD-vol. 143, ASME, New York, 1992, pp. 7–24.
[22] T. Nomura, ALE finite element computations of fluid–structure interaction problems, Comput. Methods Appl. Mech. Engrg. 112 (1994) 291–308.
[23] J.R. Womersley, Method for the calculation of velocity, rate of flow and viscous drag in arteries when the pressure gradient is known, J. Physiol. 127 (1955) 553–563.
[24] F. Otto, Die grundform des arteriellen pulses, Z. Biol. 37 (1899) 483–586.
[25] K. Hayashi, H. Handa, S. Nagasawa, A. Okumura, K. Moritake, Stiffness and elastic behavior of human intracranial and extracranial arteries, J. Biomech. 13 (1980) 175–184.